

# Heralded Emission Detection in Quantum Dot Solids under Twin-Photon Excitation

Chieh Tsao<sup>1,2</sup>, Xiang Li<sup>3,4</sup>, Alex Hinkle<sup>1</sup>, Yifan Chen<sup>1</sup>, Elvar Oskarsson<sup>1</sup>, Uri Banin<sup>3,4</sup>, Hendrik Utzat<sup>1,2\*</sup>

<sup>1</sup> Department of Chemistry, University of California, Berkeley, California 94720, USA

<sup>2</sup> Materials Science Division, Lawrence Berkeley National Lab, Berkeley, California 94720, USA

<sup>3</sup> Institute of Chemistry, The Hebrew University of Jerusalem, Jerusalem 91904, Israel

<sup>4</sup> The Center for Nanoscience and Nanotechnology, The Hebrew University of Jerusalem, Jerusalem 91904, Israel

\* [hutzat@berkeley.edu](mailto:hutzat@berkeley.edu)

## Abstract

Harnessing quantum correlations between photons is an emerging direction in optical spectroscopy, but experimental progress has thus far been limited to fluorescence-detected studies of molecular systems at room temperature. Here, we demonstrate heralded emission detection (HED) under continuous-wave (CW) entangled-photon excitation of near-infrared (NIR)-emitting colloidal III–V quantum dots (QDs) at low temperatures. We use superconducting nanowire single-photon detectors (SNSPDs) and large-area NIR avalanche photodiodes (APDs) to maximize the time resolution ( $\sim 70$  ps) and emission count rates ( $\sim 2000$  cps). To our knowledge, these results represent the first demonstration of HED in the solid state and establish NIR QDs as a bright, tunable model system with longer-lived coherences and integrability with optical cavities as an additional experimental control knob.

## 1 Introduction

Optical spectroscopy continues to illuminate foundational processes in chemical, biomolecular, and solid-state systems across timescales. Thus far, canonical optical spectroscopy uses classical light from pulsed or continuous-wave (CW) lasers producing coherent wavepackets or wavetrains. The conventional semiclassical description for the light-matter interaction, treating light as a classical perturbation of a quantum system, is therefore typically sufficient [1, 2]. Electronic or vibrational coherences generated through pulse/sample interaction can be interfered with additional time-delayed optical pulses, thereby bestowing non-linear spectroscopy with exquisite control via the bandwidth, shape, and delay between pulses [3]. These control knobs

can extract the energy-time correlations of a sample response without requiring any quantization of field excitations, i.e., without invoking photons.

A relatively new paradigm in optical spectroscopy uses quantum light i.e., photons with defined correlations in time, energy, or polarization [4, 5]. This is distinctly different from classical spectroscopy, where coherent laser light is characterized by a Poissonian number distribution of otherwise uncorrelated photons [6, 7]. Quantum spectroscopy can therefore use what classical spectroscopy cannot; the inherent correlations between photons in bespoke quantum states. Recent theoretical efforts have explored non-classical correlations between photons in spectroscopic experiments e.g., using energy-time entangled pairs. Intriguing theoretical predictions [4] beyond overcoming classical noise limits have been made [8]. For instance, access to classically forbidden excitation pathways [9], control over photo-chemical conversion rates through vibrational wavepacket preparation [10, 11], or remote-controlled spectroscopy via twin-pair detection of entangled states have been proposed [12].

Only a few experimental studies on entangled-photon light-matter interaction follow the theoretical lead. As such, the optical response of materials and molecules under quantum light excitation, e.g., single-photon Fock states or energy-time entangled photon pairs from spontaneous parametric downconversion (SPDC) has gradually come into focus [13, 14], but is still limited by the significant experimental complexity of quantum light spectroscopy. In this context, the still-limited brightness of entangled photon sources used for sample excitation is a particular challenge [15]. This is different from most spectroscopic experiments, in which sample stability rather than the achievable excitation power is the limiting factor. Probing sample coherences after entangled-photon interaction with the sample using a 'probe' pulse (or second photon) is therefore not easily achieved due to the low probability of two photons interacting with the same emitter. Instead, either the entangled photon phase delay (in transmission) or spontaneous emission as proxy for entangled photon absorption is measured.

Two common entangled two-photon (ETP) spectroscopies include fluorescence-detected two-photon absorption [16, 17, 18] and heralded emission detection (HED) [19, 20, 21, 22, 23]. Two-photon absorption using ETP has been reported to exhibit stronger absorption compared to classical two-photon absorption, owing to the intrinsic time correlation of photons in pairs [16]. This effect has potential applications in fluorescence microscopy [17], although it remains somewhat debated [24]. HED leverages the intrinsic time correlation of photon pairs from quantum light sources such as SPDC. One photon excites the emissive sample, while its twin is directly detected to "herald" the excitation event. Correlating the herald with the following photoluminescence photon reconstructs the emission dynamics, using the twin-pair correlations. This is fundamentally different from the laser-pulse correlations employed in conventional lifetime measurements using time-correlated single-photon counting (TCSPC). HED lifetime measurements therefore work with pulsed

and CW lasers. The wavelengths of the entangled photons can be finely tuned by adjusting the temperature of the nonlinear crystal in the SPDC process, allowing for wavelength-dependent excitation studies. Because SPDC produces photon statistics in each arm that follow a thermal distribution, HED can be employed to study emission lifetimes under thermal light-like conditions. This makes it especially valuable for exploring systems such as photosynthetic complexes or photovoltaic materials under illumination with realistic underlying photon statistics. Another key difference is that TCSPC requires very low detection probability per pulse (1–5%) to avoid pile-up, which limits usable counts [25]. HED, not tied to an excitation clock, avoids pile-up and can in principle operate at higher fluxes. Despite its conceptual simplicity, only a few studies have applied HED, all of which have measured solution-phase molecular systems such as Indocyanine Green (ICG) [19], Rhodamine 6G (R6G) [20], and IR-140 [23]. A noteworthy feature of HED is its ability to herald single-photon Fock states to study light-driven processes in the ultimate limit of excitation intensity, e.g., in Light-Harvesting 2 (LH2) complexes [21, 22].

To advance quantum spectroscopy, both the scope of accessible methods and samples must be expanded. HED’s current main limitation, shared with all other entangled-pair spectroscopy, is the low photon flux and coincidence rates from entangled-photon sources. HED is therefore currently not competitive for routine lifetime measurements. However, it can provide a foundation for extending quantum-light spectroscopy beyond simple intensity correlations, opening the possibility to resolve additional energy- and polarization-correlations. Such capabilities would enable more sophisticated approaches for probing quantum systems, with the broader aim of accessing entanglement signatures and unraveling excitonic dynamics in quantum materials [26]. In light of these requirements, the expansion of entangled-pair spectroscopy from solution-phase organic molecules to solid-state materials is a logical next step. First, the entangled light-matter interaction and emission can be photonicly enhanced to increase both the overall brightness and excitation rate per emitter. The latter is needed, for example, to validate theoretical predictions of inter-pair delay-dependent two-photon excitation i.e., electronic pathway selectivity [27]. To advance quantum spectroscopy, both the scope of accessible methods and samples must be expanded. HED’s current main limitation, shared with all other entangled-pair spectroscopy, is the low photon flux and coincidence rates from entangled-photon sources. HED is therefore currently not competitive for routine lifetime measurements. However, it can provide a foundation for extending quantum-light spectroscopy beyond simple intensity correlations, opening the possibility to resolve additional energy- and polarization-correlations. Such capabilities would enable more sophisticated approaches for probing quantum systems, with the broader aim of accessing entanglement signatures and unraveling excitonic dynamics in quantum materials [26]. In light of these requirements, the expansion of entangled-pair spectroscopy from solution-phase organic molecules to solid-state materials is a logical next step. First, the entangled light-matter interaction and emission can be photonicly enhanced

to increase both the overall brightness and excitation rate per emitter. The latter is needed, for example, to validate theoretical predictions of inter-pair delay-dependent two-photon excitation i.e., electronic pathway selectivity [27].

Here, we demonstrate HED in solid-state materials at low temperatures, specifically thin-films of near-infrared (NIR) emitting colloidal InAs/ZnSe quantum dots (QDs). QDs offer a rich platform for exploring entangled-pair light-matter interactions, thanks to their tunable electronic fine structure, phonon coupling, and electron-hole radiative and non-radiative rates [28]. To our knowledge, our results represent the first demonstration of entangled-photon heralded emission detection in a solid-state material, distinct from prior two-photon excitation approaches using entangled photons [29]. QD’s processability and proven integration with nanophotonic structures may help overcome brightness limitations through enhancement of the absorption and emission [30], and serve as a model system for entangled-photon non-linear spectroscopy.

## 2 Result

We developed an improved HED apparatus capable of operating over variable solid-state sample temperatures, as shown in Fig. 1a. A detailed description of the setup components is provided in the Supporting Information. Briefly, entangled photon pairs are generated via SPDC by pumping a periodically poled potassium titanyl phosphate (ppKTP) crystal with a 405 nm CW laser under the type-II phase-matching condition. The generated pairs exhibit a bandwidth of  $\sim 2$  nm with spectral overlap consistent with degenerate SPDC (Fig. 1b). A Hong-Ou-Mandel (HOM) visibility of 86% confirms the high indistinguishability of the photon pairs, in agreement with previous reports (Fig. S1) [31]. The two photons are separated by a fiber-coupled polarization beam splitter (PBS), yielding a heralding arm and a sample arm. The heralding photons are directly detected by an SNSPD, while the sample-arm photons are sent through a 50:50 beamsplitter into a cryostat with a 0.9 numerical aperture (NA) cryo-objective to excite the sample. The resulting emission is collected by the same objective, filtered from the excitation photons, and coupled via a fiber collimator into a second SNSPD. The use of SNSPDs is a notable feature of our apparatus due to their high photo-detection efficiency in the NIR ( $\sim 80\%$ ), minimal dark counts ( $< 10$  Hz), and low dead time ( $\leq 35$  ns). Their additionally low timing jitter (31 ps and 50 ps) provides an overall narrow ( $\sim 72$  ps) instrument response function (IRF) for coincidence counts without sample (Fig. 1c). The IRF width is mainly determined by the convolution of the timing jitter of the SPDC source, SNSPDs, and the single-photon counting module (19 ps).

We selected colloidal InAs/ZnSe core-shell QDs as the model system for HED. These QDs are promising NIR emitters[32] and are also widely applied in photonic devices such as photoconductors[33], phototransistors[34], and photodiodes[35, 36]. Importantly, colloidal InAs QDs can be directly deposited onto photonic platforms[37],

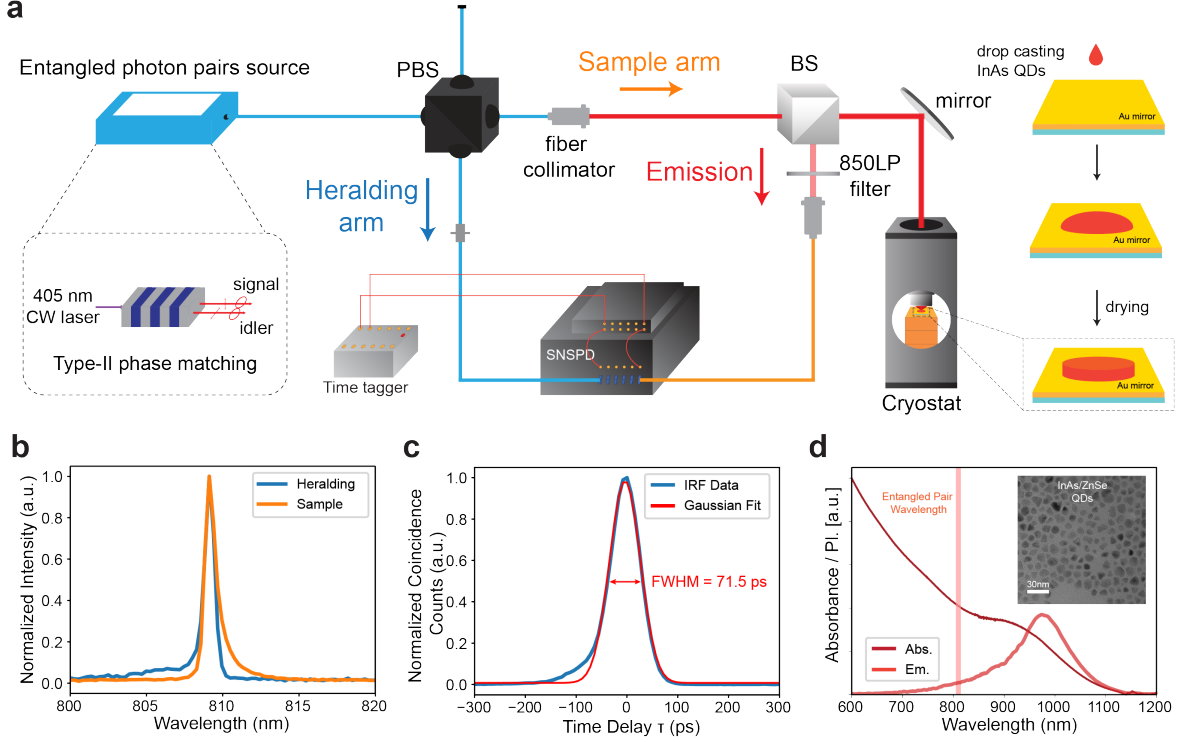


Figure 1: **Experimental setup, source characteristics, and properties of InAs/ZnSe nanocrystals.** (a) Experimental setup for heralded emission detection and preparation of InAs/ZnSe quantum dot (QD) films. (b) Normalized spectra of the entangled photons from Type-II SPDC used in the heralding and sample arms. (c) The impulse response function (IRF), obtained by replacing the sample with a cover slip coated with a thin gold film and collecting the reflected photons. (d) Ensemble absorption and emission spectra of InAs/ZnSe QDs dispersed in toluene at room temperature. The shaded region marks the twin-pair excitation wavelength in HED. For clarity, the excitation line is drawn with exaggerated width and does not represent the actual narrow bandwidth. Inset: representative transmission electron microscopy (TEM) images of InAs/ZnSe QDs. Scale bar: 30 nm.

offering a straightforward route toward integration with quantum photonic structures for optical communication and emerging quantum photonic applications.

Our synthesized type-I heterostructured InAs/ZnSe core-shell nanocrystals display high (approximately 58%) ensemble photoluminescence quantum yield (PLQY) in solution, consistent with previously reported values for this material system [38]. This PLQY is substantially higher than of organic dyes in the NIR [39], rendering NIR-QDs a natural choice for HED with high signal strengths. Room temperature QDs ensemble absorption and emission spectra reveal a low prominence excitonic shoulder around 899 nm based on Elliott model fitting (Fig. S3) and a redshifted, broad emission around 984 nm, shown in Fig. 1d. We attribute the absence of narrower features to inhomogeneous broadening due to size- and shape-inhomogeneity, which is common even for the currently best InAs QDs [32, 40]. The transmission electron microscopy (TEM) image, as shown in the inset of Fig. 1d, confirms the tetrahedral QD shape [38] and a mean particle size of  $8.2 \pm$

2.2 nm (Fig. S3). This size is only a fraction of the InAs bulk Bohr radius of around 35 nm [41], rendering our QDs well within the strong confinement regime, where size dispersion has a high impact on spectral broadening[32].

For emissive thin-film preparation, we employed drop-casting onto gold-coated coverslips (Fig. 1a) rather than conventional spin coating. Spin-coated films typically yield thin layers ( $\sim 30\text{--}100$  nm) [42, 43], which contain only a limited number of QDs within the optical focal volume (Rayleigh length  $\times$  focus spot size), thereby reducing the probability of photon absorption. Consequently, the detected HED signals can be weak even for materials with high PLQY. One strategy to increase film thickness is to mix QDs with polymers such as polystyrene or poly(methyl methacrylate). However, achieving a thickness comparable to the Rayleigh length requires a high polymer concentration, which increases the polymer-to-QD ratio within the focal volume, reduces film brightness, and may introduce non-negligible quenching effects (see Supporting Information). In principle, higher QD loadings could offset this issue, but in practice such concentrations are difficult to achieve. Another potential approach is layer-by-layer deposition, in which oleic acid-capped QDs are sequentially coated, the surface wetting properties are modified via solid-state ligand exchange, and additional layers are deposited. While this method can produce multilayered QD films [44], it often comes at the expense of reduced PLQY and requires further optimization [43]. By contrast, drop-casting naturally produces thicker and denser films, thereby improving absorption efficiency and yielding stronger HED signals. The drawback, however, is that drop-cast films typically exhibit non-uniform coverage, as shown in Fig. S3. Representative SEM images, also in Fig. S3, further highlight their inhomogeneous morphology. This inhomogeneity makes it challenging to systematically study the relationship between film brightness and thickness.

Fig. 2 illustrates the concept, stability of emission, and different approaches for analyzing HED data. Three photon “arms” are considered in the measurement: the heralding arm, the sample arm used to excite the sample, and the emission arm, which collects photons emitted by the sample following excitation. SPDC sources are not ideal [45]; in addition to generating true coincidence photon pairs, non-coincidence pairs are also produced, as shown in Fig. 2a. Consequently, the emitted sample photons originate from both non-coincidence and coincidence pairs. The former produces accidental heralding-emission coincidences. The sample emission count rates remained stable over the course of the experiment ( $\sim 15\text{--}18$  hours), confirming the sample’s stability under low excitation fluences (see Fig. 2b for 4.7 K and Fig. S4 for all temperatures). At 4.7 K, the heralding arm consistently recorded an average count rate of  $\sim 3.2 \times 10^6$  counts per second (cps). Assuming the sample arm exhibits a similar rate, and accounting for losses through optical elements, the number of excitation photons reaching the sample is estimated to be  $1.12 \times 10^6$ , corresponding to a photon power of  $\sim 275$  fW. Emitted photons were collected at a rate of  $\sim 89$  cps (see Supporting Information

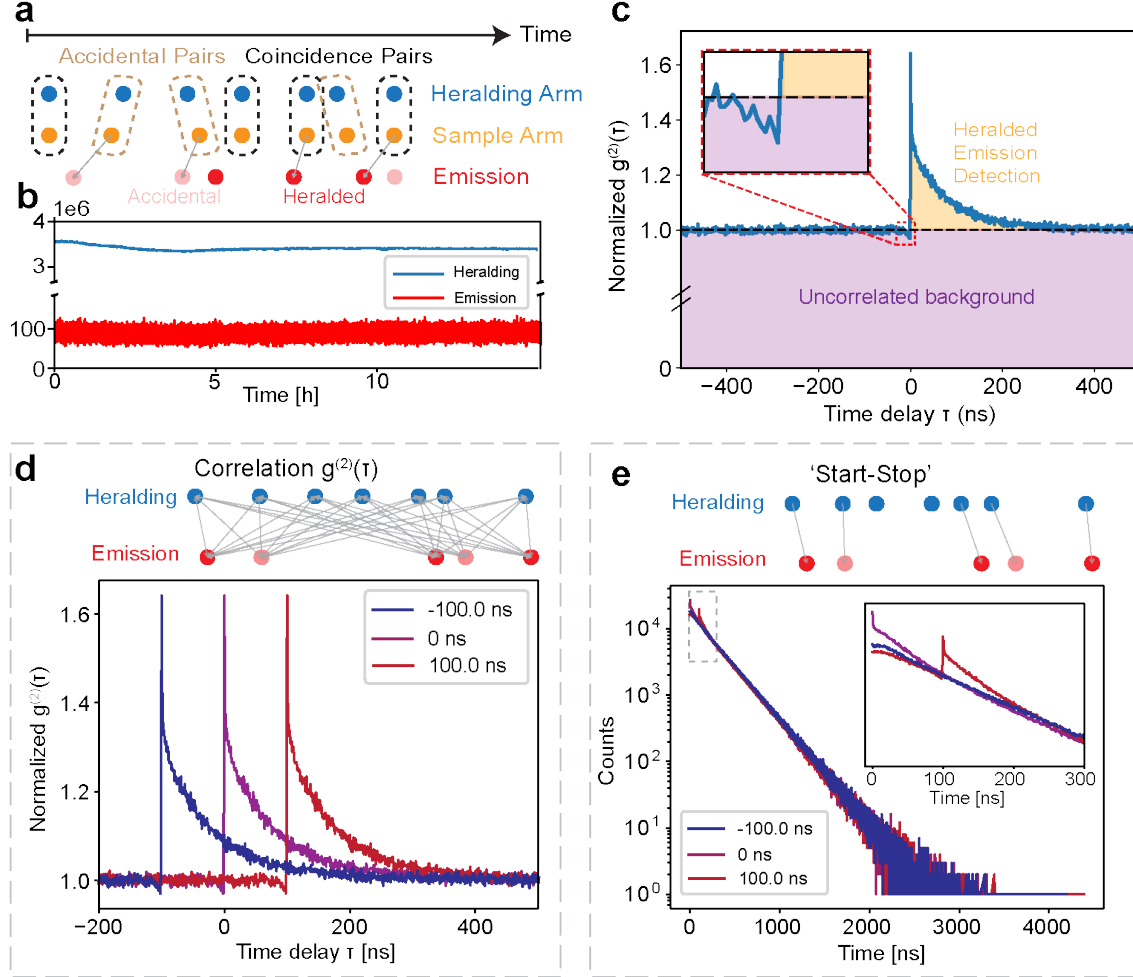


Figure 2: **Data analyses in heralded emission detection.** (a) In heralded emission detection (HED), photon pairs are split into a heralding arm (blue) and a sample arm (orange). Pairs can be classified as coincidence pairs, which are time-correlated and produce bunching in the  $g^{(2)}(\tau)$ , or non-coincidence pairs, which contribute uncorrelated background. The sample emission therefore possesses a similar statistics with emission photon from both twins (red) and accidental pairs (light red). (b) Intensity traces of the heralding arm and the emission signal during a 20h measurement at 4.7 K, demonstrating stable down-conversion over a ten-hour period. (c) Normalized cross-correlation  $g^{(2)}(\tau)$  between the heralding arm and the emission at 4.7 K. The orange-shaded region corresponds to contributions from correlated heralding-emitted photon pairs (entangled two-photon down-conversion), while the purple region represents uncorrelated background with  $g^{(2)}(\tau) = 1$ . (d) Schematic for the  $g^{(2)}$  correlation analysis of time-tagged HED data. Delaying one sequence relative to the other only shifts the bunching peak without changing its shape. (e) Schematic of the effect of adopting a 'start-stop' alternative from time-correlated single-photon counting (TCSPC) to HED, introducing distortions.

for all temperatures and details).

We now analyze correlations between heralding and sample photons, extending approaches previously applied to molecular dyes at room temperature [19, 21, 20, 23, 22]. Leveraging the short 70 ps IRF of our SNSPDs, we resolve the normalized cross-correlation  $g^{(2)}(\tau)$  between emission and heralding photons (Fig. 2c). As expected, a distinct bunching peak  $> 1$  at  $\tau = 0$  indicates preservation of the bunched statistics of twin pairs in the heralded emission. The background with  $g^{(2)}(\tau) = 1$  results from accidental coincidence events. The decay of  $g^{(2)}(\tau) > 1$  with  $\tau$  measures the effective delay between heralded photon absorption and emission, i.e. the spontaneous emission lifetime [19]. We confirm the near-equivalency of HED lifetimes of our QDs and TCSPC, as shown in the Supporting Information. Small deviations are most likely due to differences in the excitation wavelength or small deviations in setup alignments between different excitation sources. Interestingly, we identify a consistent dip of  $g^{(2)} < 1$  for  $\tau < 0$  (Fig. 2c, inset). Such anti-correlations would be consistent with time reversal symmetry breaking, but likely have a more trivial origin. We assign the origin of this dip to a non-obvious artifact from detector deadtime. Coincidences with  $\tau < 0$  are from emitted photons leading heralding photons. A leading emitted photon has a larger than random probability of being led by a second, even earlier heralding photon. The detection of this second, earliest, heralding photon turns the heralding arm SNSPD dark deadtime ( $< 20$  ns). The number of following emission/heralding coincidences within the deadtime is thus reduced, producing the dip in  $g^{(2)}(\tau < 0)$ . This artifact may be misinterpreted or may go unnoticed, especially for longer deadtime detectors. While the above correlation analysis is established, we like to point out that translation of the “start-stop” paradigm used in pulsed-laser TCSPC would require correction in post-processing and is more prone to distortion from pathlength differences. We clarify this in Fig. 2d-e.

The start-stop algorithm selects a photon on one channel as “start” and a photon on the other channel as “stop,” storing their time differences in a histogram. By contrast, the correlation algorithm accumulates all time differences between detection events on the two channels into a histogram, treating every click as both “start” and “stop,” and calculating both positive and negative delays. Using a start-stop scheme in HED can introduce distortions, since the overall number of pairs along the lifetime not only depends on the heralding ratio and entanglement time, but also the waiting time distribution of the accidental pairs. This can produce spurious accidental coincidences that are difficult to separate from the lifetime decay. Timing misalignment between emitted photon and their heralding photon can further deform the decay dynamics (Fig. 2d). The  $g^{(2)}$  correlation approach avoids these complications, as it does not impose fixed start/stop assignments on the photons. Any time delay between the heralding and emission arms merely shifts the correlation peak without distorting its decay dynamics (Fig. 2e). Waiting time distributions between accidental counts are naturally factored out in the normalized  $g^{(2)}$ .

One shortcoming of many SNSPDs is their single-mode fiber access [46], causing substantial insertion losses. If high count rates rather than minimal timing jitter are desirable in HED, large area APDs are preferred. Fig. 3a–c showcases HED results acquired across different temperatures using both an SNSPD (Fig. 3a) and a large-area APD (Fig. 3b–c). Although the employed APD exhibited high dark counts ( $\sim 1848$  cps), they contribute only to accidental coincidences and do not affect the shape of the bunching peak. We consistently observed total emission count rates of  $\sim 4000$  cps when accounting for accidental dark counts. Sample 1, with a quantum dot size of 8.2 nm, and Sample 2, with a size of 6.3 nm, showed similar absolute brightness despite their differing lifetimes. These detected count rates led to an increased external quantum efficiency (EQE) for the film i.e., the ratio of detected emission photons to heralded sample arm photons (Fig. 3f).

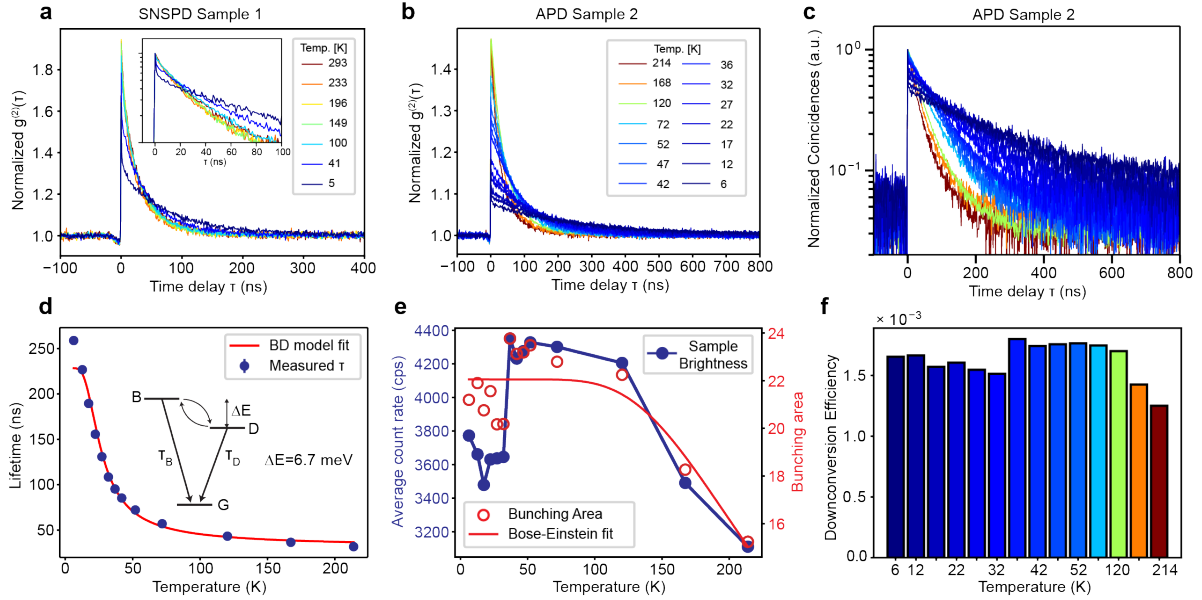


**Figure 3: Temperature-dependent HED with SNSPD and APD for sample emission detection** (a) Normalized cross-correlation  $g^{(2)}(\tau)$  at various temperatures tagging the sample emission with an SNSPD. The bunching peak reflects time correlations governed by the photoluminescence lifetime of the InAs/ZnSe quantum dots (QDs). (b) Normalized  $g^{(2)}(\tau)$  of a second QD sample measured with an avalanche photodiode (APD). (c) Data from (b) on a logarithmic scale. (d) Extracted lifetimes as a function of temperature, along with bright–dark model fits. The inset illustrates the model, where G, B, and D denote the ground, bright, and dark state, respectively. (e) Brightness and bunching peak area extracted from normalized  $g^{(2)}(\tau)$  data as a function of temperature. The bunching area is fitted with a Bose–Einstein model. (f) External quantum efficiency (EQE) of the twin photon downconversion by the sample at different temperatures, following the trend in brightness.

To demonstrate the HED analysis with these count rates, we used it to quantify temperature-dependent lifetimes. Similar to sample 1, all decay traces consistently display at least two components, independent of temperature. With increasing temperature, the fastest decay component, prominent at low temperatures,

gradually diminishes. This trend is not caused by the gold-coated substrate, as control measurements on nanocrystals deposited on plain microscope slides also exhibited the same fastest decay component, as demonstrated for sample 1 (Fig. S5). The initial fast decay component in all  $g^{(2)}$  traces is consistent with the rapid decays previously reported in InSb [47, 48] and InAs/CdSe [49] nanocrystals. Such behavior is commonly attributed either to nonradiative recombination [47, 48] or to relaxation from the bright to the dark exciton state [49]. The slower decay components are interpreted in terms of thermally activated dark-to-bright state population [50, 51], corresponding to the average lifetimes of the bright and dark exciton states. The whole lifetimes were extracted using a biexponential model for  $T \leq 52.0$  K, where one component captures the initial fast decay and the other represents the average lifetimes of the bright and dark states. At higher temperatures, where the fast component is absent, a single-exponential fit was applied to maintain consistency. This average lifetime can be interpreted as arising from two excitonic states in thermal equilibrium, separated by an energy splitting  $\Delta E$ . The dark state exhibits a longer lifetime,  $\tau_D$ , whereas the bright state has a shorter lifetime,  $\tau_B$ , in agreement with the bright-dark exciton model.

$$\tau_{avg}^{-1} = \left( \frac{e^{\Delta E/k_B T}}{1 + e^{\Delta E/k_B T}} \right) \tau_D^{-1} + \left( \frac{1}{1 + e^{\Delta E/k_B T}} \right) \tau_B^{-1} \quad (1)$$

The fitting results (Fig. 3d) yield  $\tau_D \approx 228.3$  ns,  $\tau_B \approx 16.6$  ns, and  $\Delta E \approx 6.7$  meV, values comparable to those reported for InP/ZnSe QDs [52]. The discrepancies between the data and the fit at 6.3 K, likely arise from either insufficient separation of the fastest decay component during lifetime extraction or from the need for a more comprehensive model that explicitly includes the fast component along with relaxation between bright and dark states or other contributing processes.

Fig. 3e further display the relationship between the sample brightness and the total area under the  $g^{(2)}(\tau)$  bunching peak in Fig. 3b, which both diminish with temperature. We point out that the decrease in brightness qualitatively matches a Bose-Einstein model for phonon population with a characteristic energy of  $\approx 65$  meV, consistent with phonon energies reported for III-V QDs [52, 53], possibly suggesting phonon-mediated turn-on of non-radiative decay. This effect was less pronounced in Sample 1 (Fig. S9).

### 3 Discussion

Advancing quantum spectroscopy will require both improved apparatus capabilities and broader material platforms. This study contributes by identifying colloidal InAs/ZnSe QDs as bright NIR model systems and by detailing heralding analysis, detector tradeoffs, and unexpected artifact sources to guide future improvements. The main limitation in quantum spectroscopy generally is the low coincidence rate after sample

interaction [19, 21]. Pinpointing losses to external quantum efficiency across setups [46] and materials is a logical next step. Given the tunability and integrability of QDs as photonic building blocks [54], their targeted optimization could deliver disproportionate gains.

Table 1 compares key parameters and achieved coincidence rates of all HED studies known to the authors, all but *Eshun et al.* reported low - at most around 120 - coincidence counts per second. One limitation of organic molecules is their generally decreasing luminescent quantum yield (QY) with decreasing emission energy. Few dyes in the near- and shortwave infrared have appreciable QY [39], naturally limiting the coincidence rate for molecules excitable with established sources typically operating in the NIR. *Eshun et al.* is a notable exception, producing 488–550 nm photons in the sample arm of non-degenerate SPDC pairs, enabling excitation of Rhodamine 6G with an appreciable quantum yield (95%). While this emission efficiency is certainly contributing to the suggested coincidence rate, we point out that there is currently no agreed on best practice for calculating these rates.

Our NIR QDs, used in conjunction with our setup, represent the brightest NIR samples applied to HED to date. We were unable to further improve brightness through systematic thin-film preparation, including multilayer spin-coating and the use of polymeric additives. Importantly, simply maximizing the thin-film PLQY is insufficient to predict the highest HED response, as brightness is also limited by film thickness and morphology. Thicker films can lead to reabsorption losses, while inhomogeneous films may scatter or trap emission, reducing out-coupling efficiency [55]. Thus, optimization of both absorption and emission into Gaussian-like modes, along with minimization of reabsorption in thicker films, is essential to achieve maximum HED brightness.

It is instructive to identify the limiting factors in the downconversion efficiency. Beyond the intrinsic loss from the objective’s collection efficiency, an important factor is the sample configuration—specifically, the number of QDs within the focal volume. Unlike organic dyes, QDs are physically larger, which lowers the probability of absorbing all incident photons, even though they typically exhibit higher PLQY. In addition, when using SNSPDs, the collection efficiency is constrained by the single-mode fibers [46]. While these fibers provide localized information from the film, they also introduce substantial count losses because the emission beam is imaged onto the fiber core, whereas the QD emission across the thin film is spatially inhomogeneous.

In our configuration—using an SNSPD in the heralding arm and a large-area NIR APD in the emission arm—we achieved high coincidence count rates of  $\sim 230$  coincidence counts per second (ccps) at the low temperatures. This setup maximizes detection efficiency for both herald and emitted photons while avoiding fiber-coupling insertion and losses from the incoherent sample emission into non-Gaussian modes. The trade-off, however, is the APD’s larger timing jitter, which broadens the instrument response function and reduces the precision of  $g^{(2)}(\tau)$ . These results highlight the importance of detector choice in entangled-photon

spectroscopy and suggest that advances in quantum light sources and detectors will further benefit studies of quantum light–matter interactions [15].

Overall, this study establishes colloidal QDs as a solid-state platform for exploring entangled photon light–matter interactions and for developing twin-photon detectors and entangled-photon downconversion devices. While our data do not resolve any effects of prolonged sample coherences on entangled-photon absorption, future phase-sensitive studies—such as Franson-type interferometry [56]—could directly probe entanglement preservation and benefit from the reported brightness herein.

Table 1: Summary of HED work to date

Work	Sample	Lifetime (ns)	Pump	EPP (ccps)	Excitation (cps)	Emission (cps)	Coincidences (ccps)
Harper et al. [19]	ICG	0.62	CW	–	$1 \times 10^5$	860	6.5
Li et al. [21]	LH2	1.20	Pulsed	$2.7 \times 10^5$	$9.13 \times 10^5$	–	121
Eshun et al. [20]*	R6G	3.99	CW	$1.6 \times 10^6$	–	–	23000
Gäbler et al. [23]	IR-140	0.93	CW	–	–	–	–
Alvarez-Mendoza et al. [22]	LH2	1.14	CW	$2 \times 10^5$	–	–	–
This work**	InAs/ZnSe QDs	40–250	CW	$1.6 \times 10^5$	$1.1 \times 10^6$	20–4200	4–270

Note: EPP refers to the coincidence counts per second (ccps) for entangled photon pairs. Coincidences represent counts detected between the heralding and emission arms. For comparison with the literature, we report the maximum recorded values of these counts.

\*The definitions of EPP and coincidences in some previous works may differ.

\*\*Approximations or ranges are provided for each parameter to reflect variations under different experimental conditions.

## 4 Conclusions

We have demonstrated heralded emission detection (HED) under entangled-photon excitation in InAs/ZnSe quantum dot films at cryogenic temperatures, establishing a solid-state platform for this spectroscopy. By benchmarking against TCSPC, we show that HED reliably recovers excitonic lifetimes and bright–dark state dynamics, validating its extension beyond molecular systems. Our results highlight both opportunities and limits. QDs provide brightness, tunability, and device compatibility that make them promising for quantum-light spectroscopy. While this work produced higher coincidence rates than all but one previous work [20], and the highest in the NIR spectral range, the observed coincidence rates are still modest. The demonstrated integration of QDs with optical cavities and waveguides presents a new control knob in quantum light spectroscopy, positioning QDs as a versatile model system.

## 5 Methods

### 5.1 Synthesis of InAs/ZnSe QDs

InAs/ZnSe QDs were synthesized following previously reported methods [57, 58, 59]. Both InAs nanoclusters and InAs QDs were prepared using the same precursor.

#### 5.1.1 Materials

Indium(III) acetate ( $\text{In}(\text{Ac})_3$ , 99.99% trace metals basis), oleic acid (OA, 90%), 1-octadecene (90%, ODE), tris(tri-methylsilyl) arsine (99%,  $(\text{TMS})_3\text{As}$ ), zinc stearate ( $\text{Zn}(\text{St})_2$ , 10-12% Zn basis), squalane (90%), selenium (powder, 100 mesh, 99.99% trace metals basis), toluene (anhydrous, 99.8%), ethanol (anhydrous, 99.8%) were purchased from Sigma-Aldrich. All precursors and solvents were used without further purification. All solvents were stored inside an  $\text{N}_2$ -filled glovebox.

#### 5.1.2 Synthesis of InAs Clusters

To prepare the InAs clusters solution, 12 mmol  $\text{In}(\text{Ac})_3$  and 36 mmol OA were mixed with 60 mL of ODE. The mixture was degassed at 120°C under vacuum for 90 min, then cooled down to room temperature under an Argon atmosphere. Separately, 1.6 g  $(\text{TMSi})_3\text{As}$  was mixed with 12 mL of dry ODE in the glovebox. The As solution was injected at room temperature into the indium-oleate solution with constant stirring. The reaction mixture was then heated slowly to 80°C until the solution turned dark red, indicating the formation of InAs nanoclusters. The resulting InAs nanoclusters were cooled down to room temperature and stored under an inert atmosphere in the glovebox.

#### 5.1.3 Synthesis of InAs QDs

For the synthesis of InAs QDs, 2 mmol of  $\text{In}(\text{Ac})_3$  and 6 mmol of OA were mixed together with 5 mL of ODE and left under vacuum at 120°C for 2 h. The atmosphere was then switched to argon, and the temperature was raised to 300°C. Meanwhile, 0.24 g  $(\text{TMSi})_3\text{As}$  was mixed with 2 mL of dry ODE in the glovebox. The As solution was swiftly injected into the hot indium-oleate solution at 300°C under constant stirring to initiate nucleation. The temperature was then lowered to 285°C and held constant for 20 min. During this period, aliquots were taken, and their absorption spectrum was measured. Once the first excitonic absorption peak of the seeds reached approximately 750 nm, the InAs nanoclusters solution was added continuously at a constant rate of  $2 \text{ mL}\cdot\text{h}^{-1}$ . During this reaction aliquots were taken at constant intervals to evaluate the growth and size focusing of the nanocrystals by absorption measurements. After the reaction, the mixture was cooled to room temperature and transferred into the glovebox. The resulting QDs were purified through repeated

precipitation-centrifugation-redispersion cycles using dry toluene and ethanol as solvent and antisolvent, respectively. The purified InAs QDs were finally dispersed in toluene and stored in the glovebox for further use.

#### **5.1.4 Synthesis of ZnSe shell**

To synthesize InAs/ZnSe core/shell QDs, 0.2 mmol of  $\text{Zn}(\text{St})_2$ , 3 ml squalane and the purified InAs core QDs in toluene were loaded in a 50 ml three-neck flask and degassed at 120°C under vacuum for 1 h. After purging with argon, the reaction mixture was heated up to 300°C. The Se suspension (Se-SUS, 0.2 mL, 0.5 M) was added into the solution and held at that temperature for 30 min. The temperature increased to 340 °C under argon. Maintain at this temperature for 30 minutes. Then, 0.4 mL of 0.4 M  $\text{Zn}(\text{St})_2$  suspension and 0.5 mL of 0.2 M Se-SUS solution were separately injected dropwise in the flask every 30 min. Aliquots were taken to monitor the shell growth progress. The obtained InAs/ZnSe QDs were purified with toluene and ethanol and dispersed in toluene. All the washing procedures were performed in the glovebox.

## **5.2 InAs/ZnSe QDs characterization**

The measurements of UV-vis absorption were performed on a Jasco V-570 UV-vis-NIR spectrophotometer. Photoluminescence spectra and photoluminescence quantum yield was measured by a Hamamatsu Absolute PL quantum yield spectrometer C11347-11 and Edinburgh FLS920 fluorescence spectrometer. Transmission electron microscopy (TEM) images of the InAs/ZnSe QDs were acquired using a Tecnai 12 TEM. Scanning electron microscopy (SEM) images of the QDs film were obtained with a Zeiss XB 550 FIB-SEM.

## **Acknowledgments**

We thank Tim Rambo and Ryan Wilson for helpful discussions on instrumentation. This work was financially supported by the College of Chemistry at the University of California, Berkeley and the US Department of Energy (DE-AC02-05CH11231).

## **Supplemental document**

The data supporting the findings of this study are available within the article and its Supplementary Information.

## References

- [1] Marlan O Scully and M Suhail Zubairy. *Quantum optics*. Cambridge university press, 1997.
- [2] Robert W Boyd, Alexander L Gaeta, and Enno Giese. Nonlinear optics. In *Springer Handbook of Atomic, Molecular, and Optical Physics*, pages 1097–1110. Springer, 2008.
- [3] Thomas Weinacht and Brett J Pearson. *Time-resolved spectroscopy: An experimental perspective*. CRC Press, 2018.
- [4] Konstantin E Dorfman, Frank Schlawin, and Shaul Mukamel. Nonlinear optical signals and spectroscopy with quantum light. *Reviews of Modern Physics*, 88(4):045008, 2016.
- [5] Shaul Mukamel, Matthias Freyberger, Wolfgang Schleich, Marco Bellini, Alessandro Zavatta, Gerd Leuchs, Christine Silberhorn, Robert W Boyd, Luis Lorenzo Sánchez-Soto, André Stefanov, et al. Roadmap on quantum light spectroscopy. *Journal of physics B: Atomic, molecular and optical physics*, 53(7):072002, 2020.
- [6] Anthony Mark Fox. *Quantum optics: an introduction*, volume 15. Oxford university press, 2006.
- [7] Christopher C Gerry and Peter L Knight. *Introductory quantum optics*. Cambridge university press, 2023.
- [8] Junaid Aasi, Joan Abadie, BP Abbott, Richard Abbott, TD Abbott, MR Abernathy, Carl Adams, Thomas Adams, Paolo Addesso, RX Adhikari, et al. Enhanced sensitivity of the ligo gravitational wave detector by using squeezed states of light. *Nature Photonics*, 7(8):613–619, 2013.
- [9] Ashok Muthukrishnan, Girish S Agarwal, and Marlan O Scully. Inducing disallowed two-atom transitions with temporally entangled photons. *Physical review letters*, 93(9):093002, 2004.
- [10] Bing Gu, Daniel Keefer, Flavia Aleotti, Artur Nenov, Marco Garavelli, and Shaul Mukamel. Photoisomerization transition state manipulation by entangled two-photon absorption. *Proceedings of the National Academy of Sciences*, 118(47):e2116868118, 2021.
- [11] Bo Zhou, Tse-Min Chiang, Oleg Varnavski, Sajal Kumar Giri, Chanchal Rani, George C Schatz, and Theodore Goodson III. Enhanced photochemical reaction rates with entangled photons. *The Journal of Physical Chemistry Letters*, 16(18):4372–4381, 2025.
- [12] Yuta Fujihashi, Kuniyuki Miwa, Masahiro Higashi, and Akihito Ishizaki. Probing exciton dynamics with spectral selectivity through the use of quantum entangled photons. *The Journal of Chemical Physics*, 159(11), 2023.

- [13] Christophe Couteau. Spontaneous parametric down-conversion. *Contemporary Physics*, 59(3):291–304, 2018.
- [14] Ali Anwar, Chithrabhanu Perumangatt, Fabian Steinlechner, Thomas Jennewein, and Alexander Ling. Entangled photon-pair sources based on three-wave mixing in bulk crystals. *Review of Scientific Instruments*, 92(4), 2021.
- [15] Chieh Tsao, Haonan Ling, Alex Hinkle, Yifan Chen, Keshav Kumar Jha, Zhen-Li Yan, and Hendrik Utzat. Enhancing spectroscopy and microscopy with emerging methods in photon correlation and quantum illumination. *Nature Nanotechnology*, pages 1–16, 2025.
- [16] Ryan K Burdick, George C Schatz, and Theodore Goodson III. Enhancing entangled two-photon absorption for picosecond quantum spectroscopy. *Journal of the American Chemical Society*, 143(41):16930–16934, 2021.
- [17] Oleg Varnavski and Theodore Goodson III. Two-photon fluorescence microscopy at extremely low excitation intensity: The power of quantum correlations. *Journal of the American Chemical Society*, 142(30):12966–12975, 2020.
- [18] Bing Gu and Shaul Mukamel. Manipulating two-photon-absorption of cavity polaritons by entangled light. *The Journal of Physical Chemistry Letters*, 11(19):8177–8182, 2020.
- [19] Nathan Harper, Bryce P Hickam, Manni He, and Scott K Cushing. Entangled photon correlations allow a continuous-wave laser diode to measure single-photon, time-resolved fluorescence. *The Journal of Physical Chemistry Letters*, 14(25):5805–5811, 2023.
- [20] Audrey Eshun, Xiyu Yi, Ashleigh Wilson, Sam Jeppson, Jae Hyuck Yoo, Shervin Kiannejad, Mike Rushford, Tiziana Bond, and Ted Laurence. Fluorescence lifetime measurements using photon pair correlations generated via spontaneous parametric down conversion (spdc). *Optics Express*, 31(16):26935–26947, 2023.
- [21] Quanwei Li, Kaydren Orcutt, Robert L Cook, Javier Sabines-Chesterking, Ashley L Tong, Gabriela S Schlau-Cohen, Xiang Zhang, Graham R Fleming, and K Birgitta Whaley. Single-photon absorption and emission from a natural photosynthetic complex. *Nature*, 619(7969):300–304, 2023.
- [22] Raúl Álvarez-Mendoza, Lorenzo Uboldi, Ashley Lyons, Richard Cogdell, Giulio Cerullo, and Daniele Faccio. Entangled-photon time-and frequency-resolved optical spectroscopy. *arXiv preprint arXiv:2505.02940*, 2025.

- [23] Tobias B Gäbler, Patrick Then, Christian Eggeling, Markus Gräfe, Nitish Jain, and Valerio F Gili. Benchmarking of fluorescence lifetime measurements using time-frequency correlated photons. *Methods in Microscopy*, 2(1):133–145, 2025.
- [24] Bryce P Hickam, Manni He, Nathan Harper, Szilard Szoke, and Scott K Cushing. Single-photon scattering can account for the discrepancies among entangled two-photon measurement techniques. *The Journal of Physical Chemistry Letters*, 13(22):4934–4940, 2022.
- [25] Joseph R. Lakowicz. *Principles of Fluorescence Spectroscopy*. Springer, New York, 3rd edition, 2006.
- [26] Erhan Saglamyurek, Neil Sinclair, Jeongwan Jin, Joshua A Slater, Daniel Oblak, Félix Bussieres, Mathew George, Raimund Ricken, Wolfgang Sohler, and Wolfgang Tittel. Broadband waveguide quantum memory for entangled photons. *Nature*, 469(7331):512–515, 2011.
- [27] Yuta Fujihashi, Akihito Ishizaki, and Ryosuke Shimizu. Pathway selectivity in time-resolved spectroscopy using two-photon coincidence counting with quantum entangled photons. *The Journal of Chemical Physics*, 160(10), 2024.
- [28] Debasis Bera, Lei Qian, Teng-Kuan Tseng, and Paul H Holloway. Quantum dots and their multimodal applications: a review. *Materials*, 3(4):2260–2345, 2010.
- [29] Raj Pandya, Patrick Cameron, Chloé Vernière, Baptiste Courme, Sandrine Ithurria, Alex Chin, Emmanuel Lhuillier, and Hugo Defienne. Towards robust detection of entangled two-photon absorption. *arXiv preprint arXiv:2410.06199*, 2024.
- [30] Mengyu Chen, Lihua Lu, Hui Yu, Cheng Li, and Ni Zhao. Integration of colloidal quantum dots with photonic structures for optoelectronic and optical devices. *Advanced Science*, 8(18):2101560, 2021.
- [31] CI Osorio, N Sangouard, and Robert Thomas Thew. On the purity and indistinguishability of down-converted photons. *Journal of Physics B: Atomic, Molecular and Optical Physics*, 46(5):055501, 2013.
- [32] Houman Bahmani Jalali, Luca De Trizio, Liberato Manna, and Francesco Di Stasio. Indium arsenide quantum dots: an alternative to lead-based infrared emitting nanomaterials. *Chemical Society Reviews*, 51(24):9861–9881, 2022.
- [33] Tianshuo Zhao, Nuri Oh, Davit Jishkariani, Mingliang Zhang, Han Wang, Na Li, Jennifer D Lee, Chenjie Zeng, Manisha Muduli, Hak-Jong Choi, et al. General synthetic route to high-quality colloidal iii–v semiconductor quantum dots based on pnictogen chlorides. *Journal of the American Chemical Society*, 141(38):15145–15152, 2019.

- [34] Jong-Ho Kim, Byung Ku Jung, Su-Kyung Kim, Kwang-Ro Yun, Junhyuk Ahn, Seongkeun Oh, Min-Gyu Jeon, Tae-Ju Lee, Seongchan Kim, Nuri Oh, et al. Ultrasensitive near-infrared inas colloidal quantum dot-znon hybrid phototransistor based on a gradated band structure. *Advanced Science*, 10(18):2207526, 2023.
- [35] Min-Jae Choi, Laxmi Kishore Sagar, Bin Sun, Margherita Biondi, Seungjin Lee, Amin Morteza Najjariyan, Larissa Levina, F Pelayo García de Arquer, and Edward H Sargent. Ligand exchange at a covalent surface enables balanced stoichiometry in iii–v colloidal quantum dots. *Nano letters*, 21(14):6057–6063, 2021.
- [36] Bin Sun, Amin Morteza Najarian, Laxmi Kishore Sagar, Margherita Biondi, Min-Jae Choi, Xiyan Li, Larissa Levina, Se-Woong Baek, Chao Zheng, Seungjin Lee, et al. Fast near-infrared photodetection using iii–v colloidal quantum dots. *Advanced Materials*, 34(33):2203039, 2022.
- [37] Ali W Elshaari, Wolfram Pernice, Kartik Srinivasan, Oliver Benson, and Val Zwiller. Hybrid integrated quantum photonic circuits. *Nature photonics*, 14(5):285–298, 2020.
- [38] Dongxu Zhu, Houman Bahmani Jalali, Gabriele Saleh, Francesco Di Stasio, Mirko Prato, Nefeli Polykarpou, Andreas Othonos, Sotirios Christodoulou, Yurii P Ivanov, Giorgio Divitini, et al. Boosting the photoluminescence efficiency of inas nanocrystals synthesized with aminoarsine via a znse thick-shell overgrowth. *Advanced Materials*, 35(38):2303621, 2023.
- [39] Knut Rurack and Monika Spieles. Fluorescence quantum yields of a series of red and near-infrared dyes emitting at 600- 1000 nm. *Analytical chemistry*, 83(4):1232–1242, 2011.
- [40] Theodore A Gazis, Ashleigh J Cartlidge, and Peter D Matthews. Colloidal iii–v quantum dots: a synthetic perspective. *Journal of Materials Chemistry C*, 11(12):3926–3935, 2023.
- [41] Shihai Kan, Taleb Mokari, Eli Rothenberg, and Uri Banin. Synthesis and size-dependent properties of zinc-blende semiconductor quantum rods. *Nature materials*, 2(3):155–158, 2003.
- [42] Jung Hoon Song, Hyekyoung Choi, Hien Thu Pham, and Sohee Jeong. Energy level tuned indium arsenide colloidal quantum dot films for efficient photovoltaics. *Nature communications*, 9(1):4267, 2018.
- [43] Ahmad R Kirmani, Grant Walters, Taesoo Kim, Edward H Sargent, and Aram Amassian. Optimizing solid-state ligand exchange for colloidal quantum dot optoelectronics: How much is enough? *ACS Applied Energy Materials*, 3(6):5385–5392, 2020.

- [44] Boris D Chernomordik, Ashley R Marshall, Gregory F Pach, Joseph M Luther, and Matthew C Beard. Quantum dot solar cell fabrication protocols. *Chemistry of Materials*, 29(1):189–198, 2017.
- [45] Sven Ramelow, Alexandra Mech, Marissa Giustina, Simon Gröblacher, Witlef Wieczorek, Jörn Beyer, Adriana Lita, Brice Calkins, Thomas Gerrits, Sae Woo Nam, et al. Highly efficient heralding of entangled single photons. *Optics express*, 21(6):6707–6717, 2013.
- [46] Taehyun Kim, Peter Maunz, and Jungsang Kim. Efficient collection of single photons emitted from a trapped ion into a single-mode fiber for scalable quantum-information processing. *Physical Review A—Atomic, Molecular, and Optical Physics*, 84(6):063423, 2011.
- [47] Wenyong Liu, Angela Y Chang, Richard D Schaller, and Dmitri V Talapin. Colloidal insb nanocrystals. *Journal of the American Chemical Society*, 134(50):20258–20261, 2012.
- [48] Serena Busatto, Mariska de Ruiter, Johann TBH Jastrzebski, Wiebke Albrecht, Valerio Pinchetti, Sergio Brovelli, Sara Bals, Marc-Etienne Moret, and Celso de Mello Donega. Luminescent colloidal insb quantum dots from in situ generated single-source precursor. *ACS nano*, 14(10):13146–13160, 2020.
- [49] Thomas Stanley Bischof. *On the origin of photons: understanding excitons and multiexcitons in colloidal semiconductor nanocrystals*. PhD thesis, Massachusetts Institute of Technology, 2015.
- [50] C de Mello Donegá, M Bode, and A Meijerink. Size-and temperature-dependence of exciton lifetimes in cdse quantum dots. *Physical Review B—Condensed Matter and Materials Physics*, 74(8):085320, 2006.
- [51] Dan Oron, Assaf Aharoni, Celso de Mello Donega, Jos van Rijssel, Andries Meijerink, and Uri Banin. Universal role of discrete acoustic phonons in the low-temperature optical emission of colloidal quantum dots. *Physical review letters*, 102(17):177402, 2009.
- [52] Annalisa Brodu, Mariana V Ballottin, Jonathan Buhot, Elleke J Van Harten, Dorian Dupont, Andrea La Porta, P Tim Prins, Mickael D Tessier, Marijn AM Versteegh, Val Zwiller, et al. Exciton fine structure and lattice dynamics in inp/zns core/shell quantum dots. *ACS photonics*, 5(8):3353–3362, 2018.
- [53] Annalisa Brodu, Mariana V Ballottin, Jonathan Buhot, Dorian Dupont, Mickael Tessier, Zeger Hens, Freddy T Rabouw, Peter CM Christianen, Celso de Mello Donega, and Daniel Vanmaekelbergh. Exciton-phonon coupling in inp quantum dots with zns and (zn, cd) se shells. *Physical Review B*, 101(12):125413, 2020.
- [54] Maria Ibáñez, Simon C Boehme, Raffaella Buonsanti, Jonathan De Roo, Delia J Milliron, Sandrine Ithurria, Andrey L Rogach, Andreu Cabot, Maksym Yarema, Brandi M Cossairt, et al. Prospects of nanoscience with nanocrystals: 2025 edition. *ACS nano*, 2025.

- [55] Jia-Sheng Li, Yong Tang, Zong-Tao Li, Xin-Rui Ding, Long-Shi Rao, and Bin-Hai Yu. Effect of quantum dot scattering and absorption on the optical performance of white light-emitting diodes. *IEEE Transactions on Electron Devices*, 65(7):2877–2884, 2018.
- [56] Sylvain Fasel, Franck Robin, Esteban Moreno, Daniel Erni, Nicolas Gisin, and Hugo Zbinden. Energy-time entanglement preservation in plasmon-assisted light transmission. *Physical review letters*, 94(11):110501, 2005.
- [57] Lior Asor, Jing Liu, Shuting Xiang, Nir Tessler, Anatoly I Frenkel, and Uri Banin. Zn-doped p-type inas nanocrystal quantum dots. *Advanced Materials*, 35(5):2208332, 2023.
- [58] Xiang Li, Einav Scharf, Adar Levi, Yinon Deree, David Stone, Sergei Remennik, and Uri Banin. Shell phase and morphology control for emission tuning in iii–v core/shell quantum dots. *ACS nano*, 2025.
- [59] Sudarsan Tamang, Sunghee Lee, Hyekyoung Choi, and Sohee Jeong. Tuning size and size distribution of colloidal inas nanocrystals via continuous supply of prenucleation clusters on nanocrystal seeds. *Chemistry of Materials*, 28(22):8119–8122, 2016.

## Supplementary materials

### S1 The detailed configuration of the setup

#### S1.1 Heraled Emission Detection (HED)

The entangled photon pair source (customized QES 2.4, Qubitekk) consists of a 405 nm continuous-wave (CW) laser that pumps a periodically poled potassium titanyl phosphate (ppKTP) crystal housed in a temperature-controlled oven, allowing for tuning of the photon wavelength and degree of degeneracy. The indistinguishability of photon pairs has been shown in Fig. S1. Entangled photon pairs are generated via spontaneous parametric down-conversion (SPDC), after which the residual pump light is filtered out. The entangled photons are then coupled into optical fiber. A polarization-maintaining, fiber-coupled polarizing beam splitter (PBS) with FC/PC connectors (Qubitekk) is connected to the source output to separate the signal and idler photons. One output of the PBS is routed via an FC/PC sleeve (ADAF2, Thorlabs) to a single-mode fiber patch cable (780HP, Diamond), which is terminated with an E2000 connector and connected to a superconducting nanowire single-photon detector (SNSPD, Quantum Opus), referred to as the heralding arm.

The other output of the PBS is coupled into a protected-silver-coated reflective fiber collimator (RC02FC-P01, Thorlabs), producing a collimated beam with a  $1/e^2$  diameter of approximately 1.8 mm. The beam is launched into free space, passes through an 810 nm bandpass filter (FBH810-10, Thorlabs) and protected-silver mirrors (PF10-03-P01, Thorlabs), and is elevated by a periscope assembly (RS99, Thorlabs) equipped with the same mirror type. It then passes through a 50:50 beam splitter (BS014, Thorlabs) and is directed onto an x-y galvanometric mirror system (GVS012, Thorlabs) controlled by a data acquisition (DAQ) platform (T7, LabJack). The reflected beam is subsequently relayed into a high-numerical-aperture (NA) objective (EC Epiplan-Neofluar 100 $\times$ /0.9 BD DIC M27, Zeiss) housed in a closed-cycle cryostat (Montana Instruments) using a pair of relay lenses with focal lengths of 150 mm (AC254-150-AB-ML, Thorlabs) and 200 mm (AC254-200-AB-ML, Thorlabs). This configuration, together with the beam divergence, expands the spot to fill the objective's back aperture, which has a conjugate plane size of approximately 3 mm.

Photoluminescence emission from the sample is collected by the same objective and travels back through the same relay lens pair and galvo system. The emission is separated from the excitation path by the same 50:50 BS and filtered by an 850 nm long-pass filter (FELH0850, Thorlabs) to remove residual excitation photons. The filtered emission is then collected by another fiber coupler (PAF2P-A10B FiberPort, Thorlabs) and routed via single-mode fiber patch (1060HI, Diamond) to a second SNSPD, referred to as the emission arm.

Different fibers and detectors are used for the heralding and emission arms to match their respective wavelength ranges. The Heralding arm uses 780HP fiber, which operates effectively in the 780–970 nm range, and is connected to an SNSPD with a timing jitter of approximately 31 ps, less than 1 dark count per second, and a dead time of 20 ns. The Sample arm uses HI1060 fiber, paired with an SNSPD optimized for the emission wavelength of InAs/ZnSe nanocrystals. This detector has a timing jitter of approximately 50 ps, fewer than 10 dark counts per second, and a dead time of 18 ns.

Detection events from both SNSPDs are time-stamped with 8 ps resolution using a single-photon counting module (Time Tagger Ultra, Performance Edition, Swabian Instruments). For second-order correlation measurements, the system accumulates the time differences between photon detection events on the two channels into a histogram. Each detection event is considered as both a “start” and a “stop,” allowing the calculation of both positive and negative time delays. A time bin width of 1 ns is chosen to balance the trade-off between signal-to-noise ratio (SNR) and timing resolution.

For the APD-based version of the HED, the short-pass dichroic mirror (FF825-SDI01, Semrock) replaces the PBS output path, and the signal is detected using an APD (id120, IDQ).

It should be noted that the timing jitters here are specified as full width at half maximum (FWHM).

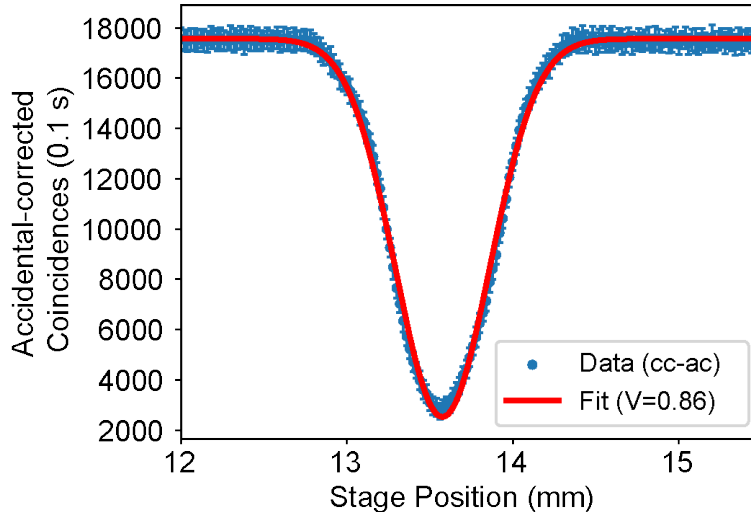


Figure S1: Hong–Ou–Mandel (HOM) dip of the entangled photon pairs, indicating their indistinguishability, with a visibility of approximately 86%.

Table S1: Summary of detectors used in this work.

Detector	Deadtime (ns)	dark count (cps)	Timing jitter (ps)	detection efficiency
SNSPD (heralding)	< 20@780 nm	< 10	31	83%@780nm
SNSPD (emission)	≤ 35@1315nm	< 10	50	83%@1064 nm
APD	400	~1848	<400	10%@1000 nm

## S1.2 Time-Correlated Single Photon Counting (TCSPC)

The setup for TCSPC measurements closely follows that used for HED, with the primary difference being the excitation source: a 470 nm pulsed laser (LDH-P-C-470, PicoQuant). The laser repetition rate is reduced to 2.5 MHz using an external controller (PDL 820, PicoQuant) to meet the desired excitation conditions. Along the excitation path, a 500 nm short-pass filter (FESH0500, Thorlabs) is combined with a set of neutral density filters (NE20B, NE20A, and NE10A-A; Thorlabs), reducing the excitation fluence to  $6.37 \text{ nJ/cm}^2$ , which cause the exciton number per pulse  $\langle N \rangle \ll 1$ . All other optical components remain unchanged from the HES setup.

For TCSPC measurements, a start-stop mode is used on the same Time Tagger in place of a second-order correlation algorithm. In this mode, detection events on two channels are recorded as start and stop signals, and the time differences between them are compiled into a histogram. For consistency with HED data, the histogram bin width is set to 1 ns.